ChemComm

Laser-induced oxygen vacancies in FeCo2O4 nanoparticles for boosting oxygen evolution and reduction

SCHOLARONE™
Manuscripts

ChemComm

COMMUNICATION

Laser-induced oxygen vacancies in $FeCo_2O_4$ nanoparticles for boosting oxygen evolution and reduction

Kang-Wen Qiu,[a] Cong Xi, [a] Yan Zhang, [a,b] Rui Zhang, [a] Zhe Li, [a] Gu-Rong Sheng, [a] Hui Liu, *[a] Cun-Ku Dong, [a] Yong-Jun Chen*[c] and Xi-Wen Du*[a]

$FeCo_2O_4$ nanoparticles with abundant oxygen vacancies were produced by laser fragmentation. The oxygen vacancies can lower the thermodynamic energy barriers as well as accelerate the electron transfer, eventually promote oxygen evolution and reduction reactions simultaneously.

Rechargeable zinc-air battery (ZAB), a green and efficient energy storage system, displays considerably high energy densities due to the utilization of oxygen in atmosphere rather than heavy reactant. The practical application of ZAB depends on the development of efficient bifunctional electrocatalysts that can efficiently drive both the oxygen evolution reaction(OER) and oxygen reduction reaction (ORR).[1-3] Although Pt-, Ru, or Ir- based materials have been widely reported as active catalysts for OER or ORR, the high price and scarcity greatly limit their widespread application.[4] MCo_2O_4 (M=Ni, Mn, Fe, Zn, and so on) materials with a spinel structure have been conceived as promising alternatives because of their low cost and abundant resource.[5-9] However, the poor electrical conductivity and low catalytic activity prevent MCo_2O_4 from being applied in ZABs. Recently, great progress has been made on improving the electrical conductivity of MCo_2O_4 by compositing them with carbon materials,[10,11] which inspires the passion on exploiting more efficient strategies to boost their conductivity.

Introducing oxygen vacancies in oxides has been accepted as a promising way to improve the catalytic activity for both OER and ORR.[12,13] Commonly, the oxygen vacancies were generated by annealing in hydrogen, which is unsafe and energy hungry.[14] In a previous work, we reported top-down synthesis of Co_3O_4 nanoparticles (NPs) by laser fragmentation, and found that this technique exhibis a quick heating-queching feature which favors the formation of oxygen vacancies.[15] However, the catalytic activity of Co_3O_4 NPs, especially for ORR, is not high enough to meet the needs of ZABs. Meanwhile, the universality of the laser technique on generating defects has not been investigated carfully. Therefore, it is fascinating to find out potential bifunctional (OER and ORR) catalysts whose activities could be promoted by laser fragmentation.

Herein, we show that $FeCo_2O_4$, a typical MCo_2O_4 spinel, is suitable for generating oxygen vacancies by laser fragmetation. We employ an intensive pulsed laser to break $FeCo_2O_4$ microsphere (M-$FeCo_2O_4$) into a large amount of ultrafine $FeCo_2O_4$ NPs rich in oxygen vacancies (R-$FeCo_2O_4$). The ultrasmall size and abundant oxygen vacancies jointly improve the electron transfer and catalytic activity for OER and ORR. As the air cathode of ZAB, R-$FeCo_2O_4$ achieves high power density and long lifetime, even outperforming noble metal Pt/C+RuO_2 couple.

The synthesis process is schematically shown in Fig. S1, where M-$FeCo_2O_4$ was partially vaporized and broken via trival fragmentation under laser irradiation.[15, 16] giving rise to numerous tiny R-$FeCo_2O_4$ nanoparticles (see Fig. S2). The morphology and structure of as-prepared R-$FeCo_2O_4$ NPs were examined by transmission electron
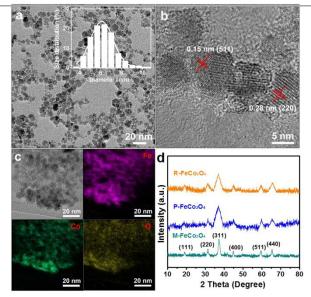

Fig. 1. Morphology and structure of R-$FeCo_2O_4$. (a), (b) Low and high magnification TEM images of R-$FeCo_2O_4$, respectively; (c) STEM elemental mapping of R-$FeCo_2O_4$; (d) XRD patterns of R- $FeCo_2O_4$, P-$FeCo_2O_4$ and M-$FeCo_2O_4$.

[a]Institute of New-Energy Materials, School of Materials Science and Engineering, Tianjin Unviersity, Tianjin 300072, P.R. China. E-mail: liu_hui@tju.edu.cn, xwdu@tju.edu.cn,

[b]Stanford Synchrotron Radiation Lightsource, SLAC National Accelerator Laboratory, Menlo Park, California 94025, USA.

[c]State Key Laboratory of Marine Resource Utilization in South China Sea, School of Materials Science and Engineering, Hainan University, Haikou 570228, China. Email:yongchen@hainu.edu.cn,
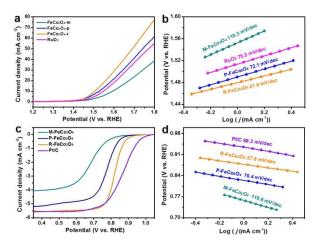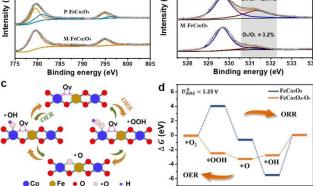
Fig. 2. Electrochemical performance of OER and ORR. (a) LSV curves and (b) Tafel plots for the catalytic OER process of R-FeCo$_2$O$_4$, P-FeCo$_2$O$_4$, M-FeCo$_2$O$_4$, and RuO$_2$; (c) LSV curves and (d) Tafel plots for the catalytic ORR process of R-FeCo$_2$O$_4$, P-FeCo$_2$O$_4$, M- FeCo$_2$O$_4$, and Pt/C.

Fig. 3. Characterizations on oxygen vacancies and their influence on catalytic activities of R-FeCo$_2$O$_4$. (a) Fitted Co 2p spectra for R-FeCo$_2$O$_4$, P-FeCo$_2$O$_4$ and M-FeCo$_2$O$_4$; (b) Fitted O 1s spectra for R-FeCo$_2$O$_4$, P-FeCo$_2$O$_4$ and M- FeCo$_2$O$_4$; (c) The OER/ORR mechanism of R-FeCo$_2$O$_4$ with oxygen vacancy (O$_v$); (d) DFT diagram of perfect FeCo$_2$O$_4$ and R-FeCo$_2$O$_4$.

microscope (TEM) and X-ray diffraction (XRD). As shown in Fig. 1a, R-FeCo$_2$O$_4$ NPs are well dispersed with an average size of 6.5 nm. In high resolution TEM image of Fig. 1b, some lattices are observed with spacings of 0.28 and 0.15 nm, corresponding to (220) and (511) planes of FeCo$_2$O$_4$, respectively.[17] The scanning transmission electron microscopy (STEM) elemental mapping analysis clearly shows uniform distribution of iron, cobalt and oxygen elements in R-FeCo$_2$O$_4$ NPs (Fig. 1c). For comparison, we also prepared FeCo$_2$O$_4$ NPs poor in oxygen vacancies (P-FeCo$_2$O$_4$) under the same laser fragmentation conditions excpept for in oxygen atmosphere. P-FeCo$_2$O$_4$ NPs display similar uniformity and size distribution with R-FeCo$_2$O$_4$ NPs (Fig. S3). In addition, the X-ray diffraction (XRD) patterns of R-FeCo$_2$O$_4$, P-FeCo$_2$O$_4$ and M-FeCo$_2$O$_4$ shown in Fig. 1d are indexed to cubic spinel phase FeCo$_2$O$_4$.[18]

We then tested the OER properties of R-FeCo$_2$O$_4$, with P-FeCo$_2$O$_4$, M-FeCo$_2$O$_4$ and RuO$_2$ as the references. Linear-sweep voltammogram (LSV) curves in Fig. 2a indicate that R-FeCo$_2$O$_4$ delivers an overpotential of 276 mV at the current density of 10 mA cm^{-2}, this value is much lower than those of P-FeCo$_2$O$_4$ (297 mV), M-FeCo$_2$O$_4$ (363 mV) and RuO$_2$ (319 mV). The tafel slopes also confirmed the superior OER activity of R-FeCo$_2$O$_4$. As shown in Fig. 2b, R-FeCo$_2$O$_4$ affords a low Tafel slope of 61.6 mV dec^{-1} compared with P-FeCo$_2$O$_4$ (72.1 mV dec^{-1}), M-FeCo$_2$O$_4$ (115.2 mV dec^{-1}) and RuO$_2$ (75.2 mV dec^{-1}). In addition, R-FeCo$_2$O$_4$ displays high stablity, the current density merely decreases by 4 % after testing for 20 h (Fig. S4). These results are superior to those of nonprecious metal-based oxide catalysts reported in literature (Table S1).

ORR plays a critical role during the discharge process of ZAB. Fig. 2c show LSV curves of the above four catalysts on rotating disk electrode (RDE) in O$_2$-saturated 0.1 M KOH at a scan rate of 5 mV·s^{-1} and 1600 rpm. The onset potential and the half-wave potential of R-FeCo$_2$O$_4$ are 0.95 and 0.82 V, respectively, much higher than these of M-FeCo$_2$O$_4$ (0.86 and 0.68 V). Meanwhile, as shown in Fig. 2d, R-FeCo$_2$O$_4$ shows smaller Tafel slope (57.8 mV dec^{-1}) relative to P-FeCo$_2$O$_4$ (70.4 mV dec^{-1}), M-FeCo$_2$O$_4$ (110.6 mV dec^{-1}) and even Pt/C (68.3 mV dec^{-1}). LSVs at different rotating rates were shown in Figs. S5a-S5d, the electron transfer numbers (n) during the ORR process

can be evaluated by the fitted Koutecky-Levich (K-L) plots (Figs. S5e and S5f). R-FeCo$_2$O$_4$ exhibits a high electron transfer number of 3.87 which is close to that of Pt/C (3.9), indicating a dominant four-electron process. Rotating ring-disk electrode (RRDE) measurements were carried out to monitor the hydrogen peroxide yield (% H$_2$O$_2$), as shown in Fig.S6. The H$_2$O$_2$ yield of R-FeCo$_2$O$_4$ ranges from 5% to 7% and the calculated electron-transfer number is above 3.84, which is similar to the results obtained from the K-L plots. Moreover, the long term durability is tested at 0.5 V for 20 h, as shown in Fig. S7, R-FeCo$_2$O$_4$ exhibits the best catalytic stability. Although the onset potential of R-FeCo$_2$O$_4$ is still worse than Pt/C (1.04 V), the Tafel slope and limited current density of R-FeCo$_2$O$_4$ is comparable to Pt/C and among the top values achieved by transition-metal-based oxide catalysts (Table S2).

To understand the performance improvement of R-FeCo$_2$O$_4$, we performed XPS measurements on the three FeCo$_2$O$_4$ samples. In Fig.3a, O1s spectra can be fitted with two peaks at 529.7 and 531.3 eV, respectively. The peak at 529.7 eV arise from lattice oxygen (O$_L$), whereas the peak at 531.3 eV is attributed to adsorbed oxygen on oxygen vacancy (O$_V$).[13-15] Obviously, the O$_V$/O$_L$ ratio of R-FeCo$_2$O$_4$ (46.7%) is much higher than those of P-FeCo$_2$O$_4$ (29.1%) and M-FeCo$_2$O$_4$ (3.2%), suggesting more oxygen vacancies were generated in R-FeCo$_2$O$_4$ by laser fragmentation. According to the fine-scanned Co 2p XPS spectra given in Fig. 3b, the majority of cobalt cations in FeCo$_2$O$_4$ samples are present in Co^{3+} form. As compared with the other two samples, R-FeCo$_2$O$_4$ shows higher peak related to Co^{2+} ions which have been proved as the catalytic active sites for ORR.[19] In combination with the results in Figs. 3a and 3b, introducing oxygen vacancies benefits the formation of Co^{2+} cations in FeCo$_2$O$_4$. Moreover, electron paramagnetic resonance (EPR) was employed to detect the oxygen vacancies. As shown in Fig. S8, R-FeCo$_2$O$_4$ displays an intensive EPR signal at g-value of 2.002 related to the unpaired electrons trapped by oxygen vacancies. [20] This signal is greater than those of M-FeCo$_2$O$_4$ and P-FeCo$_2$O$_4$, confirming that R-FeCo$_2$O$_4$ possesses more oxygen vacancies than M-FeCo$_2$O$_4$ and P-FeCo$_2$O$_4$.

Next, we carried out density functional transformation (DFT) calculation to analyse the influence of oxygen vacancies on the

catalytic process. Both OER and ORR involve four elementary reaction steps (Fig. 3c and S9). In the ORR process, O_2 molecules were adsorbed on the surface of catalysts and reduced into *OOH, followed by further reduction to *O, *OH and H_2O in sequence; while OER proceeds in the reverse direction. The free energy diagrams were obtained by the DFT calculation and shown in Fig. 3d, where a large thermodynamic barrier (ΔG) can be found for the formation of *OOH on the perfect $FeCo_2O_4$ surface without oxygen vacancies. After introducing oxygen vacancies into R-$FeCo_2O_4$, this ΔG value is significant reduced, thus facilitating the ORR and OER processes. The significant reduced of ΔG value of *O reduction to *OOH, and *OOH reduction to O_2, means the higher efficient for four-electron dominant process, which is conformed to the results from K-L plots. Therefore, DFT results certify the critical role of oxygen vacancies on improving ORR and OER catalytic activities of $FeCo_2O_4$.

To understand the superior performance of R-$FeCo_2O_4$, electrochemically active surface area (ECSA) and electrochemical impedance spectrum (EIS) were further conducted. As shown in Fig. S10, ECSA of R- $FeCo_2O_4$ is 62.5 cm^2, which is higher than that of P-$FeCo_2O_4$ (40.1 cm^2) and M-$FeCo_2O_4$ (10.8 cm^2). Because the similar size distribution of R-$FeCo_2O_4$ and P-$FeCo_2O_4$, the higher ECSA of R-$FeCo_2O_4$ should arise from the improved catalytic activity by introdcing oxygen vacancies. In addtion to the intrinsic activity, the electrical conductivity is also crucial on the catatytic performance. Hence, we employed electrochemical impedance spectrum (EIS) to investigate the electron transfer. EIS of the R- $FeCo_2O_4$, P-$FeCo_2O_4$ and M-$FeCo_2O_4$ were measured at a potential of 1.6 V with an AC perturbation of 5 mV in the frequency range from 0.01 Hz to 100 KHz. Fig. S11 presents the Nyquist plots which were fitted with an equivalent circuit as shown in inset. The Rs mainly results from the solution resistance. The charge transfer resistance (Rct=R1+R2), which can be interpreted as the Faradaic process and oxygen-species adsorption, respectively. The Rct value of R-$FeCo_2O_4$ is smallest, R-$FeCo_2O_4$ displays the smallest Rct value among the three samples, implying that oxygen vacancies can lower the charge transfer resistance at the interface between catalyst and electrolyte. Besides, more sample with different amount of oxygen vacancies were synthesized and tested the catalytic performance, the results indicated the catalytic activity could improve with the oxygen vacancies increased (Fig. S12).

Finally, we constructed a ZAB with R-$FeCo_2O_4$ as the air cathode, zinc plate as the anode and 6.0 M KOH as the electrolyte (Fig. 4a). For comparison, coupled commercial Pt/C+RuO_2 catalyst was also tested as the air cathode. The R-$FeCo_2O_4$ battery worked stably with a high open-circuit voltage of 1.44 V (Fig. S9a) which is very close to that of Pt/C+RuO_2 (1.46 V). The charging and discharging curves of ZABs are shown in Fig. 4b, R-$FeCo_2O_4$ presents similar cell voltages at the low current density with Pt/C+RuO_2. As the current exceeds 70 mA cm^{-2}, the charging and discharging voltages of the R-$FeCo_2O_4$ ZAB are superior to the noble-metal ZAB, indicating that the R-$FeCo_2O_4$ cathode is more active than the Pt/C+RuO_2 couple. Fig. 4c shows typical discharging polarization curves and the corresponding power density plots of the ZABs. R-$FeCo_2O_4$ based ZAB exhibits a significant superior performance in terms of current density and power density (140 mW cm^{-2} at a current density of 210 mA cm^{-2}). Moreover, the R-
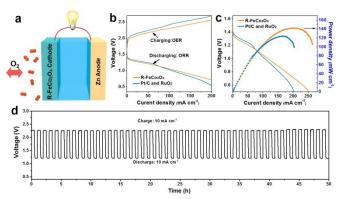

Fig. 4. Electrochemical performance of ZABs. (a) Schematic of the primary Zn-air battery; (b) Charge and discharge polarization curves of R-$FeCo_2O_4$ and Pt/C+RuO_2 batteries; (c) Polarization curves and corresponding power-density plots of R-$FeCo_2O_4$ and Pt/C+RuO_2 batteries; (d) Cycling performance of the R-$FeCo_2O_4$ battery.

$FeCo_2O_4$ ZAB was cycled for 50 h at a charge and discharge current density of 10 mA cm^{-2} to test long-term durability of ZABs. As shown in Figure 4d, after 50 cycles, there is no visible increase in the voltage gap, indicating excellent durability of the R-$FeCo_2O_4$ ZAB. The superior discharge rate performance (Fig. 13b) demonstrated the R-$FeCo_2O_4$ ZAB can be operated at a wide range of current densities. Moreover, the R-$FeCo_2O_4$ ZAB can discharge more than 200 h with a discharge voltage of 1.15 V, and the capacity reaches 589 mA h g^{-1} at 20 mA cm^{-2} (Figs. S13c, S13d).

In conclusion, the ultrafine $FeCo_2O_4$ nanoparticles with abundant oxygen vacancies were successfully fabricated by laser fragmentation. The catalytic activity for both OER and ORR were remarkably improved by the abundant oxygen vacancies. The catalyst was used as the air cathode for zinc-air battery, exhibiting the high power density and long cycling performance. This work provides a new strategy towards highly active bifunctional catalysts based on defect engineering.

Conflicts of interest

The authors declare no conflict interests.

Notes and references

1. X. Liu, M. Park, M. G. Kim, S. Gupta, G. Wu and J. Cho, *Angewandte Chemie International Edition*, 2015, **54**, 9654-9658.

2. J. Fu, X. P. Song, H. Zarrin, X. F. Tian, J. L. Qiao, L. Rasen and Z. W. Chen, *Energy & Environmental Science*, 2016, **9**, 663-670.

3. D. S. He, D. He, J. Wang, Y. Lin, P. Yin, X. Hong, Y. Wu and Y. Li, *Journal of the American Chemical Society*, 2016, **138**, 1494-1497.

4. C. Y. Su, H. Cheng, W. Li, Z. Q. Liu, N. Li, Z. F. Hou, F. Q. Bai, H. X. Zhang and T. Y. Ma, *Advanced Energy Materials*, 2017, **7**, 1602420.

5. X. Liu, M. Park, M. G. Kim, S. Gupta, X. J. Wang, G. Wu and

J. Cho, *Nano Energy*, 2016, **20**, 315-325.

6.   C. Z. Yuan, H. B. Wu, Y. Xie and X. W. Lou, *Angewandte Chemie International Edition*, 2014, **53**, 1488-1504.

7.   T. F. Hung, S. G. Mohamed , C. C. Shen, Y. Q. Tsai, W. S. Chang and R. S. Liu, *Nanoscale*, 2013, **5**, 12115-12119.

8.   Q. Wang, L. Shang, R. Shi, X. Zhang, Y. F. Zhao, G. I. N. Waterhouse, L. Z. Wu, C. H. Tung and T. R. Zhang, *Advanced Energy Materials*, 2017, **7**, 1700467.

9.   Z. Q. Liu, H. Cheng, N. Li, T. Y. Ma and Y. Z. Su, *Advanced Materials*, 2016, **28**, 3777-3784.

10.   S. Gadipelli, T. T. Zhao, S. A. Shevlin, Z. X. Guo, *Energy & Environmental Science*, 2016, **9**,1661-1667.

11.   T. T. Zhao, S. Gadipelli, G. J. He, M. J. Ward, D. Do, P. Zhang, Z. X. Guo, *CHEMSUSCHEM*, 2018, **11**, 1295-1304.

12.   J. Bao, X. D. Zhang, B. Fan, J. J. Zhang, M. Zhou, W. L. Yang, X. Hu, H. Wang, B. C. Pan and Y. Xie, *Angewandte Chemie International Edition*, 2015, **127**, 7507-7512.

13.   J. Guo, S. Gadipelli, Y. C. Yang, Z. N. Li, Y. Lu, D. J. L. Brett, Z. X. Guo, *Journal of Materials Chemistry A*, 2019, **8**, 3544-3551.

14.   T. Zhai, S. L. Xie, M. H. Yu, P. P. Fang, C. L. Liang, X. H. Lu and Y. X. Tong, *Nano Energy*, 2014, **8**, 255-263.

15.   Y. Zhou, C. K. Dong, L. L. Han, J. Yang and X. W. Du, *ACS Catalysis*, 2016, **6**, 6699-6703.

16.   J. Yang, T. Ling, W. T. Wu, H, Liu, M. R. Gao, C.Ling, L. Li and X. W. Du, *Nature Communication*, 2013, **4**, 1695.

17.   S. G. Mohamed, C. J. Chen, C. K. Chen, S. F. Hu and R. S. Liu, *ACS Applied Materials Interfaces*, 2014, **6**, 22701-22708.

18.   B. G. Zhu, S. C. Tang, S. Vongher, H. Xie and X. K. Meng, *ACS Applied Materials Interfaces*, 2016, **8**, 4762-4770.

19.   Y. Y. Liang, H. L. Wang, J. G. Zhou, Y. G. Li, J. Wang, T. Regier and H. J. Dai, *Journal of the American Chemical Society*, 2012, **134**, 3517-3523.

20.   Y. T. Wang, J. M. Cai, M. Q. Wu, J. H. Chen, W. Y. Zhao, Y. Tian, T. Ding, J. Zhang, Z. Jiang and X. G. Li, *Applied Catalysis B: Environmental*, 2018, **239**, 398-407.